# Submodule Capacitance Monitoring Strategy for Phase-Shifted Carrier Pulse-Width Modulation Based Modular Multilevel Converters

Liu, Chengkai; Deng, Fujin; Yu, Qiang; Wang, Yanbo; Blaabjerg, Frede; Cai, Xu

*Published in:*
I E E E Transactions on Industrial Electronics

*DOI (link to publication from Publisher):*
10.1109/TIE.2020.3014572

*Publication date:*
2021

*Document Version*
Accepted author manuscript, peer reviewed version

# Submodule Capacitance Monitoring Strategy for Phase-Shifted Carrier Pulse-Width Modulation Based Modular Multilevel Converters

Chengkai Liu, Fujin Deng, *Senior Member, IEEE*, Qiang Yu,
Yanbo Wang, *Senior Member, IEEE*, *Frede Blaabjerg*, *Fellow, IEEE* and Xu Cai

***Abstract***- The capacitance monitoring is one of the important issues for the MMC to obtain high reliability. Since the pulse-width modulation (PWM) is usually implemented in the Field Programmable Gate Array (FPGA), the produced precise switching states in the FPGA cannot be directly access by the top Digital Signal Processor (DSP) controller, which poses challenges on the existing capacitance monitoring methods based on the precise switching states of the MMC. This paper presents a submodule (SM) capacitance monitoring strategy for the MMC with a simple algorithm, where the fundamental frequency components of the SM capacitor voltage and current are extracted to estimate the SM capacitance based on reference, but not the precise switching states. The proposed scheme not only simplifies the implementation and calculation, but also avoids control limitations and heavy communication burden between DSP and FPGA. Besides, the proposed strategy effectively eliminates noise impact from sensors and increases accuracy. Simulation and experimental studies are implemented, and the results confirm the effectiveness of the proposed strategy.

***Index terms*—Capacitance monitoring, modular multilevel converters, reliability, PSC-PWM, submodule**

## I. Introduction

The modular multilevel converter (MMC) has drawn considerable interests due to its advantages of modularity, scalability, high efficiency, low harmonic content and fault tolerance [1]-[3]. A multilevel voltage can be synthetized with the operation of the MMC and the SM switching frequency can be reduced without compromising the power quality [4]. Recently, the MMC is more attractive for renewable energy integration, medium-voltage motor drives, and electric railway supplies [5]-[7].

The capacitor is one of the fragile components in the MMC [8]. Due to high energy density and low price [9], the electrolytic capacitor is popular for MMCs in some applications, such as micro-grids, motor drives and front-end rectifier [10]-[12]. Owing to vaporization of the electrolyte, the capacitor would gradually deteriorate and capacitance would be changed [13]. Normally, the capacitor is required to be replaced with a new one when its capacitance drops below 80% of rated value [14]. As a result, it's essential to monitor the SM capacitance value for reliable operation.

Recently, several SM capacitance monitoring methods have been reported for MMCs, which can be divided into direct monitoring methods and indirect monitoring methods. The direct monitoring methods are based on precise capacitor voltage and current. Reference [15] presents a direct capacitor monitoring method for the MMC, where each SM capacitance is estimated by a recursive least square (RLS) algorithm. However, an ac current is required to be injected into the circulating current in [15], which increases the arm current and affects the MMC performance. In [16]-[19], the SM capacitance is estimated using band-pass filters and root mean square (RMS) calculations. However, a double frequency circulating current injection is required in [16] and the methods in [17]-[19] are only suitable for the MMC without circulating current suppression control (CCSC). Besides, the Kalman filter (KM) algorithm [20] and fast-affine projection (FAP) algorithm [21] are adopted to estimate the SM capacitance in MMCs. In [22], a new non-contact current sensor is implemented to extract the SM capacitor current and RLS algorithm is adopted to estimate the capacitance. The direct monitoring methods in [15]-[21] are based on capacitor voltages, arm current and SM switching states, whose estimation errors are usually below 1%. However, in some applications, the precise switching states cannot be directly access by the controller, thus the methods in [15]-[21] would have trouble in practical application.

The indirect monitoring methods are other solutions for capacitance estimation in the MMC, which are based on the relationships among the SM capacitances. Reference [23] estimates the capacitance based on the relationship between the arm average capacitance and the capacitance of each SM. Reference [24] presents a reference SM (RSM) based capacitance monitoring method to reduce computational burden, where the reference SM is employed to estimate the capacitances in other SMs. Reference [25] presents an improved RSM based capacitance estimation method, which makes full use of the voltage sensor measurement range to improve accuracy. However, two SMs have to be out of service during the monitoring period. Reference [26] presents

This work was supported in part by the National Natural Science Foundation of China under Project 61873062 and in part by the Natural Science Foundation of Jiangsu Province under Project BK20180395. *(Corresponding author: Fujin Deng.)*

C. Liu and Q. Yu are with School of Electrical Engineering, Southeast University, Nanjing 210096, China (e-mail: lckisafish@163.com; yyuqiang@163.com).

F. Deng is with the School of Electrical Engineering, Southeast University, and Jiangsu Key Laboratory of Smart Grid Technology and Equipment, Nanjing 210096, China (e-mail: fdeng@seu.edu.cn).

Y. Wang and F. Blaabjerg are with the Department of Energy Technology, Aalborg University, Aalborg 9220, Denmark (e-mail: ywa@et.aau.dk; fbl@et.aau.dk).

X. Cai is with the Wind Power Research Center, Shanghai Jiao Tong University, Shanghai 200240, China (e-mail: xucai@sjtu.edu.cn).

a sorting-based capacitance monitoring method to reduce computational burden in the MMC with a large number of SMs, where only the SM with the smallest capacitance is judged and estimated. In [27], the monitored SM is controlled to be bypassed from the arm and the capacitor is discharged through the bleeding resistor, where the time of the capacitor voltage decreasing to a predefined value is used to estimate the SM capacitance. Reference [28] presents a capacitance monitoring method based on the relationship between phase current and capacitor voltage, but only during the DC-side start-up procedure. Reference [29] presents a capacitance monitoring method for MMCs with nearest level modulation (NLM) based on the relationship between SM voltage variation and SM driving signal angle. In indirect methods, the precise switching states of the SMs are not required, thus the indirect methods are easier to implement than the direct methods.

For the MMC system with a number of SMs, the typical implementation architecture is composed of the DSP and FPGA. The DSP is normally used to implement the control algorithm, while the FPGA is used to produce the switching states based on the modulation references received from the DSP. The existing capacitor monitoring methods require the precise SM switching states [15]-[21]. It means that the DSP is required to receive the precise SM switching states produced in the FPGA for the implementation of capacitor monitoring algorithm in the DSP, which would be difficult for the DSP to have such a high sampling speed and such a large calculation amount.

In this paper, a SM capacitance monitoring strategy is proposed for the phase-shifted carrier (PSC) pulse-width modulation (PWM) based MMC, where the fundamental frequency components of SM capacitor voltage and current are extracted to estimate the SM capacitance. The advantages of the proposed strategy are: 1) It does not require SM switching states, but only the references. It can be directly implemented in the DSP controller, avoid fast sampling and transmission of precise switching states from FPGA to DSP controller, and greatly reduce computational burden in comparison with [15]-[21]. 2) It has the feature of noise immunity, which increases the accuracy of the capacitance monitoring in comparison with [24] and [27]. 3) It has no extra control or effect on control performance and is more practical for implementation in comparison with [15], [17], [24] and [27].

The rest of the paper is organized as follows. Section II introduces the basic principles of the MMC. The proposed SM capacitance monitoring strategy is presented in Section III. And the discussion of the proposed strategy is presented in Section IV. Then, simulation studies and experimental studies are respectively given in Section V and Section VI to verify the effectiveness of the proposed capacitance monitoring strategy. Finally, the conclusions are drawn in Section VII.

## II. Modular Multilevel Converters

Fig. 1(a) shows a three-phase MMC, which consists of phase A, phase B and phase C. The subscript $u$ refers to the upper arm while the subscript $l$ refers to the lower arm. Each phase is composed of an upper arm and a lower arm, which contains an arm inductor $L_s$ and $n$ identical SMs in series. Fig. 1(b) shows the diagram of the $i$-th SM in the upper arm of phase A, which is composed of upper switch/diode $T_1/D_1$, lower switch/diode $T_2/D_2$, and the capacitor $C_{aui}$. In normal operation, the SM is controlled by a switching function $S_{aui}$, as

$$S_{aui}=\begin{cases}1, & T_1 \text{ is switched on and } T_2 \text{ is switched off}\\ 0, & T_1 \text{ is switched off and } T_2 \text{ is switched on}\end{cases}. \quad (1)$$

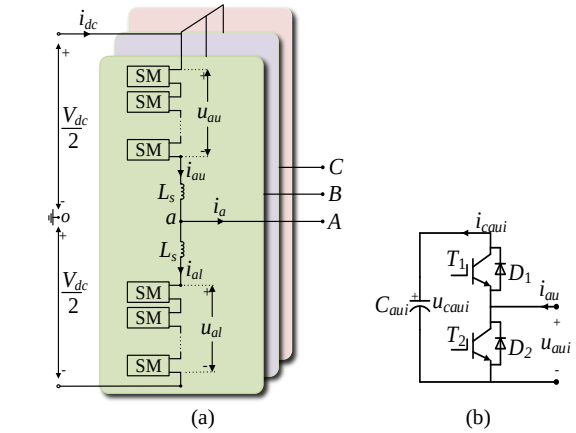


Fig. 1. (a) Three-phase MMC. (b) The $i$-th SM in upper arm of phase A.

## III. Proposed Capacitance Monitoring Strategy For MMCs under PSC-PWM

### A. PSC-PWM Based Control System of MMCs

Fig. 2 shows a typical implementation architecture for the MMC based on DSP and FPGA [30], [31]. The DSP mainly realizes control algorithm such as output current control, voltage balancing control, CCSC, capacitance monitoring, protection and user interface based on the signals such as capacitor voltages, arm currents and grid voltages received from the FPGA. Based on the produced reference signal from the DSP, the FPGA generates the switching signals for each SM based on the PWM scheme.

In the DSP shown in Fig. 2, the arm reference $y_{au}$ is generated based on the output current control such as the active power, reactive power and dc-link voltage regulation. To guarantee each capacitor voltage balancing, the PSC-PWM

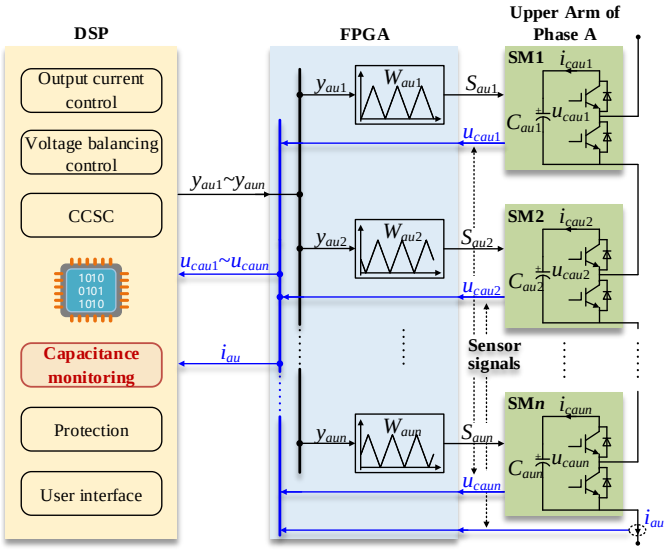


Fig. 2. Typical implementation architecture of MMCs based on DSP and FPGA.

based individual capacitor voltage balancing control is implemented. Owing to that the semiconductor stress and the power absorbed by the SMs are evenly distributed in the MMC under PSC-PWM, each SM capacitor voltage can be easily kept balanced [31]. According to [31], the balancing compensation component $\Delta y_{aui}$ ($i$=1, 2…$n$) for the $i$-th SM is generated as

$$\Delta y_{aui} = K_p \cdot (u_{ave\_a} - u_{caui}) \cdot i_{cir\_a} \tag{2}$$

where $K_p$ is the proportional gain, $u_{ave\_a}$ is the average capacitor voltage within phase A, $i_{cir\_a}$ is the circulating current in phase A as $i_{cir\_a}=(i_{au}+i_{al})/2$ and $i_{al}$ is the lower arm current in phase A. As a result, the reference $y_{aui}$ for the $i$-th SM is

$$y_{aui} = y_{au} + \Delta y_{aui} \tag{3}$$

The $n$ references $y_{au1}$~$y_{aun}$ are sent to the FPGA by communication. In the FPGA, $n$ triangular carriers $W_{au1}$~$W_{aun}$ are generated, which are respectively shifted by $2\pi/n$. By comparing the references $y_{au1}$~$y_{aun}$ with the carriers $W_{au1}$~$W_{aun}$, respectively, the $n$ switching functions $S_{au1}$~$S_{aun}$ are generated to drive SM1~SM$n$ in the upper arm of phase A.

### B. Analysis of Capacitor Voltage and Current

In the MMC, the current in phase A can be expressed as

$$i_a = I_m \sin(\omega_0 t + \varphi) \tag{4}$$

where $I_m$ is the peak value, $\omega_0$ is the fundamental angular frequency and $\omega_0=2\pi f_0$, $f_0$ is the fundamental frequency and $\varphi$ is the power factor angle. Suppose the second-order harmonic circulating current is suppressed by the CCSC [32], according to [33], the upper arm current $i_{au}$ in phase A can be expressed as

$$i_{au} = \frac{i_a}{2} + \frac{i_{dc}}{3}. \tag{5}$$

where $i_{dc}$ is the dc-link current of the MMC.

The voltage reference for phase A can be defined as

$$u_{a\_ref} = U_m \cos(\omega_0 t + \delta). \tag{6}$$

where $U_m$ is the peak value and $\delta$ is the angle between the reference voltage and grid side voltage. The reference voltage for the upper arm of phase A is

$$u_{au\_ref} = \frac{1}{2} V_{dc} - u_{a\_ref} \tag{7}$$

where $V_{dc}$ is the dc voltage, as shown in Fig. 1(a). As a result, the arm reference for the upper arm of phase A is

$$y_{au} = \frac{u_{au\_ref}}{V_{dc}} = \frac{1}{2} - \frac{M}{2}\cos(\omega_0 t + \delta). \tag{8}$$

where $M$ is modulation index given as $M = 2U_m/V_{dc}$.

According to (5) and (8) [33], the capacitor current $i_{caui}$ in the $i$-th SM is

$$i_{caui} = y_{aui} \cdot i_{au}. \tag{9}$$

The capacitor voltages $u_{caui}$ in the $i$-th SM is

$$u_{caui} = u_{caui0} + \frac{1}{C_{aui}} \int_0^t i_{caui} \cdot dt, \tag{10}$$

where $u_{caui0}$ is the dc component of capacitor voltage.

Fig. 3(a) shows the amplitudes of the fundamental frequency component and double frequency component of capacitor current under various active power; Fig. 3(b) shows the amplitudes of the fundamental frequency component and double frequency component of capacitor voltage under various active power, whose parameters are derived from simulations in Section V. It can be observed that the fundamental frequency components in capacitor current and voltage are obviously larger than the double frequency components.

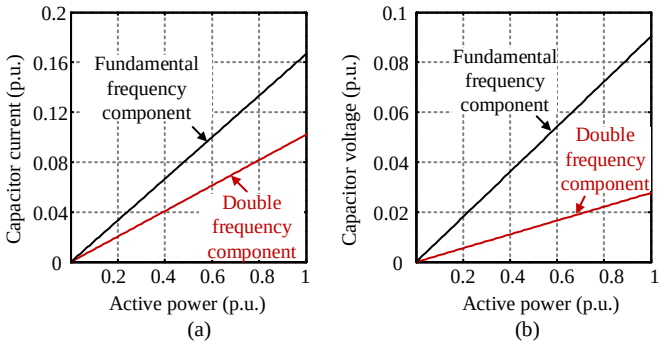


Fig. 3. Fundamental frequency components and double frequency components under various active power. (a) Capacitor current. (b) Capacitor voltage.

### C. Analysis of SM Capacitance

According to the above analysis, the fundamental frequency components at angular frequency $\omega_0$ in capacitor voltage and current are dominant, which can be used for capacitance analysis. The capacitor voltage $u_{caui}$ in (10) is multiplied by $\cos(\omega_0 t)$ and $\sin(\omega_0 t)$, respectively, and integrated in $N_T$ fundamental periods as

$$\begin{cases} A_{u\_aui} = \int_0^{N_T T} u_{caui}(t) \cdot \cos(\omega_0 t) dt \\ B_{u\_aui} = \int_0^{N_T T} u_{caui}(t) \cdot \sin(\omega_0 t) dt \end{cases}, \tag{11}$$

where $N_T$ is the number of monitoring periods. $T$ is fundamental period and $T$=1/$f_0$. The voltage coefficient $F_{u\_aui}$ is defined as

$$F_{u\_aui} = \sqrt{A_{u\_aui}^2 + B_{u\_aui}^2}. \tag{12}$$

From (11), it can be observed that when the capacitor voltage is multiplied by $\cos(\omega_0 t)$ or $\sin(\omega_0 t)$, the relationship would be as follows.

- The components in the capacitor voltage except the fundamental frequency component become alternating components, which would be eliminated in the integral process;
- The component at fundamental frequency in capacitor voltage becomes direct component, which would be accumulated in the integral process.

As a result, $F_{u\_aui}$ is only related to the fundamental frequency component in the capacitor voltage.

Similarly, the capacitor current is respectively multiplied by $\cos(\omega_0 t)$ and $\sin(\omega_0 t)$, respectively, and integrated in $N_T$ fundamental periods as

$$\begin{cases} A_{i\_aui} = \int_0^{N_T T} i_{caui}(t) \cdot \cos(\omega_0 t) dt \\ B_{i\_aui} = \int_0^{N_T T} i_{caui}(t) \cdot \sin(\omega_0 t) dt \end{cases}, \tag{13}$$

The current coefficient $F_{i\_aui}$ is defined as

$$F_{i\_aui} = \sqrt{A_{i\_aui}^2 + B_{i\_aui}^2}. \tag{14}$$

According to (9)~(14), the SM capacitance can be estimated as

$$C_{aui} = \frac{F_{i\_aui}}{\omega_0 \cdot F_{u\_aui}}. \tag{15}$$

This article has been accepted for publication in a future issue of this journal, but has not been fully edited. Content may change prior to final publication. Citation information: DOI 10.1109/TIE.2020.3014572, IEEE Transactions on Industrial Electronics

### D. Proposed Capacitance Monitoring Strategy

Based on the above analysis, a capacitance monitoring strategy is proposed, as shown in Figs. 4 and 5, which is implemented in the DSP controller shown in Fig. 2. In the proposed capacitance monitoring method, the capacitors in the arm are monitored one by one.

Figs. 4 and 5 show the proposed capacitance monitoring strategy for the $i$-th SM in the upper arm of phase A. The capacitor voltage $u_{caui}$, arm current $i_{au}$ and grid voltage $e_a$, $e_b$, $e_c$ are sampled in real-time. The phase angle $\theta$ and angular $\omega_0$ of the grid side voltage are obtained by a phase locked loop (PLL) [34]. Suppose the monitoring command is given during the period between $(j\text{-}1)T$ and $jT$, the proposed capacitance monitoring algorithm will be implemented since $jT$ and lasts for $N_T$ periods, as shown in Fig. 4.

Fig. 5 shows the implementation of the proposed capacitance monitoring algorithm for the $i$-th SM in the DSP controller, where the reference $y_{aui}$ is derived based on the system control of the MMC. After implementation of the proposed algorithm, the $A_{u\_aui}$, $B_{u\_aui}$ and $A_{i\_aui}$, $B_{i\_aui}$ can be calculated based on (11) and (13), respectively. At the end of the implementation of the proposed algorithm, as shown in Fig. 4, the voltage coefficient $F_{u\_aui}$ and current coefficient $F_{i\_aui}$ can be calculated based on (12) and (14). Then, the capacitance $C_{aui}$ in the $i$-th SM can be estimated based on (15).

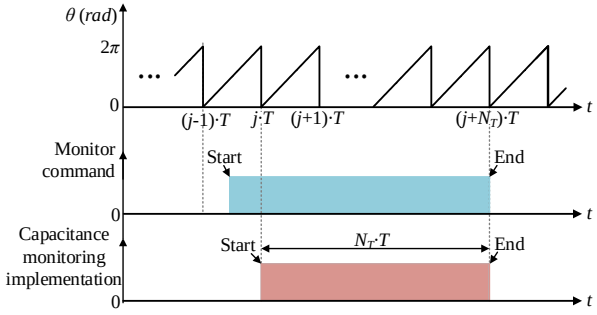


Fig. 4. Diagram of the start and end of the proposed capacitance monitoring strategy.

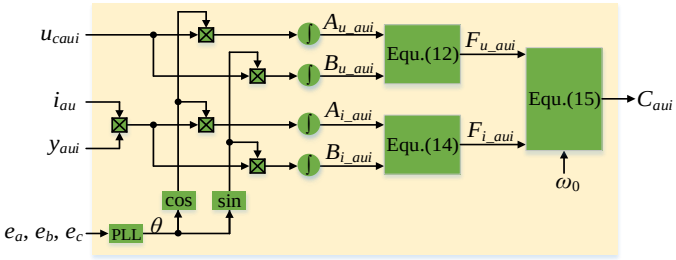


Fig. 5. Proposed capacitance monitoring strategy for the $i$-th SM in the upper arm of phase A.

## IV. Discussion of Proposed Capacitance Monitoring Strategy

### A. Analysis of Noise Immunity

To estimate the capacitances in the MMC, a large number of sensors are used for voltages and currents sampling. The measurement error is unavoidable, which would lead to inaccuracy of condition monitoring. Normally, the measurement errors mainly contain systematic errors and random errors. The systematic errors can be corrected by proofreading and compensation [35]. However, the random errors are usually caused by a variety of complex internal and external interferences during the measurement process, which are hard to avoid. The random error involved may affect the accuracy of the capacitance monitoring. Thus, the impact of the measurement error on the proposed capacitance monitoring strategy requires further investigations.

The DSP is a discrete-time controller. Considering the noise effect in a practical MMC system, the sampled $i$-th SM capacitor voltage $\hat{u}_{caui,k}$ and arm current $\hat{i}_{au,k}$ at the $k$-th control period can be respectively expressed as

$$\begin{cases} \hat{u}_{caui,k} = u_{caui,k} + v_{i,k} \\ \hat{i}_{au,k} = i_{au,k} + w_k \end{cases}, \tag{16}$$

where $v_{i,k}$ and $w_k$ are the random errors of measurement, which can be modelled as Gauss noise with the feature of being zero-mean, white and uncorrelated [36]. $v_{i,k}$ and $w_k$ obey normal distribution as

$$\begin{cases} v_{i,k} \sim N(0, \sigma_v^2) \\ w_k \sim N(0, \sigma_w^2) \end{cases}, \tag{17}$$

where $\sigma_v^2$ and $\sigma_w^2$ are the variance of $v_{i,k}$ and $w_k$, respectively. The signal-noise ratio (SNR) of the sampled capacitor voltage $\hat{u}_{caui,k}$ and current $\hat{i}_{au,k}$ are

$$\begin{cases} SNR = 20 \cdot \lg \dfrac{RMS(\hat{u}_{caui,k})}{\sigma_v} \\ SNR = 20 \cdot \lg \dfrac{RMS(\hat{i}_{au,k})}{\sigma_w} \end{cases}, \tag{18}$$

where $RMS$ is the root mean square. Along with increase of the SNR, the noise is reduced.

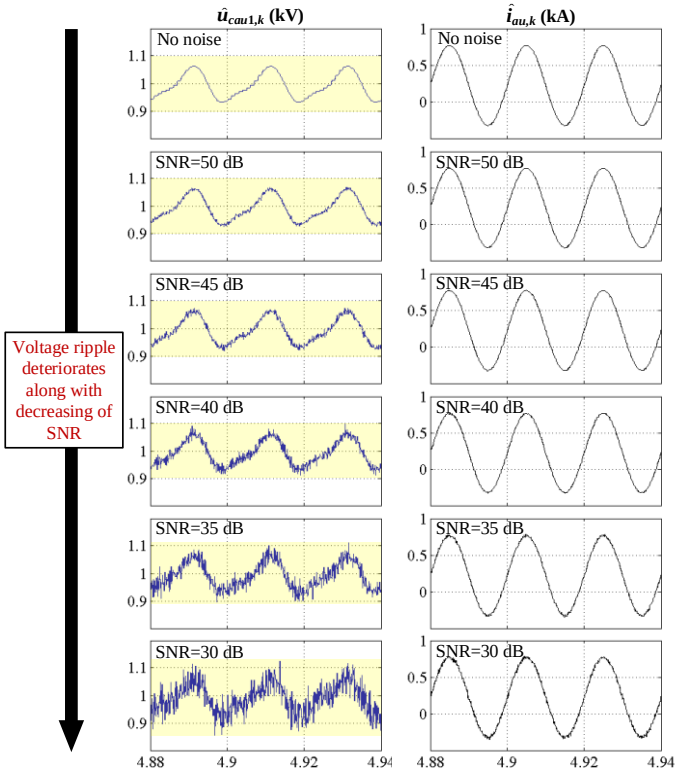


Fig. 6. Measured capacitor voltage and arm current under various SNRs.

This article has been accepted for publication in a future issue of this journal, but has not been fully edited. Content may change prior to final publication. Citation information: DOI 10.1109/TIE.2020.3014572, IEEE Transactions on Industrial Electronics

Fig. 6 shows the capacitor voltage $\hat{u}_{caui,k}$ and arm current $\hat{i}_{au,k}$ under various SNR, which are derived from case I in Section V with active power of 0.8 p.u. Here, the Gauss noise is superposed to the ideal capacitor voltage and arm current to simulate the random measurement error. In a practical system, the SNR is usually not less than 30 dB [37]. From Fig. 6, it can be observed that the noise has little effect on the arm current. However, the noise deteriorates the capacitor voltage ripple, because the capacitor voltage ripple is far smaller than the dc component in the capacitor voltage, such as typically 10% of the nominal dc component in capacitor voltage [38]. The noise deteriorates the capacitor voltage ripple along with decreasing of SNR. Consequently, it poses challenges to capacitance monitoring based on the capacitor voltage ripple.

To implement the proposed capacitance monitoring algorithm for the *i*-th SM in the discrete-time DSP controller with sampling step $T_s$, (11) and (13) are discretized as

$$\begin{cases} A_{u\_aui} = T_s \sum u_{caui,k} \cdot \cos(\theta_k) \\ B_{u\_aui} = T_s \sum u_{caui,k} \cdot \sin(\theta_k) \end{cases}, \tag{19}$$

$$\begin{cases} A_{i\_aui} = T_s \sum i_{au,k} \cdot y_{aui,k} \cdot \cos(\theta_k) \\ B_{i\_aui} = T_s \sum i_{au,k} \cdot y_{aui,k} \cdot \sin(\theta_k) \end{cases}, \tag{20}$$

Substituting (16) into (19) and (20), the $\hat{A}_{u\_aui}$, $\hat{B}_{u\_aui}$ corresponding to capacitor voltage and the $\hat{A}_{i\_aui}$, $\hat{B}_{i\_aui}$ corresponding to capacitor current can be obtained as

$$\begin{cases} \hat{A}_{u\_aui} = A_{u\_aui} + T_s \sum v_{i,k} \cos(\theta_k) \\ \hat{B}_{u\_aui} = B_{u\_aui} + T_s \sum v_{i,k} \sin(\theta_k) \end{cases} \tag{21}$$

$$\begin{cases} \hat{A}_{i\_aui} = A_{i\_aui} + T_s \sum w_k \cdot y_{aui,k} \cos(\theta_k) \\ \hat{B}_{i\_aui} = B_{i\_aui} + T_s \sum w_k \cdot y_{aui,k} \sin(\theta_k) \end{cases}. \tag{22}$$

According to (17) and (21), the relative error $e_r$ of $\hat{A}_{u\_aui}$ and $\hat{B}_{u\_aui}$ obey normal distribution as

$$\begin{cases} e_r(\hat{A}_{u\_aui}) = \dfrac{\hat{A}_{u\_aui} - A_{u\_aui}}{A_{u\_aui}} \sim N\left(0, \sigma_v^2 T_s^2 \sum \left(\dfrac{\cos\theta_k}{A_{u\_aui}}\right)^2\right) \\ e_r(\hat{B}_{u\_aui}) = \dfrac{\hat{B}_{u\_aui} - B_{u\_aui}}{B_{u\_aui}} \sim N\left(0, \sigma_v^2 T_s^2 \sum \left(\dfrac{\sin\theta_k}{B_{u\_aui}}\right)^2\right) \end{cases}. \tag{23}$$

According to (17) and (22), the relative error $e_r$ of $\hat{A}_{i\_aui}$ and $\hat{B}_{i\_aui}$ obey normal distribution as

$$\begin{cases} e_r(\hat{A}_{i\_aui}) = \dfrac{\hat{A}_{i\_aui} - A_{i\_aui}}{A_{i\_aui}} \sim N\left(0, \sigma_w^2 T_s^2 \sum \left(\dfrac{y_{aui,k}\cos\theta_k}{A_{i\_aui}}\right)^2\right) \\ e_r(\hat{B}_{i\_aui}) = \dfrac{\hat{B}_{i\_aui} - B_{i\_aui}}{B_{i\_aui}} \sim N\left(0, \sigma_w^2 T_s^2 \sum \left(\dfrac{y_{aui,k}\sin\theta_k}{B_{i\_aui}}\right)^2\right) \end{cases}. \tag{24}$$

According to (23) and (24), it can be observed that the means of $e_r(\hat{A}_{u\_aui})$, $e_r(\hat{B}_{u\_aui})$, $e_r(\hat{A}_{i\_aui})$ and $e_r(\hat{B}_{i\_aui})$ are zero respectively. In addition, $A_{u\_aui}$, $B_{u\_aui}$, $A_{i\_aui}$ and $B_{i\_aui}$ are located at denominator of the variance of $e_r(\hat{A}_{u\_aui})$, $e_r(\hat{B}_{u\_aui})$, $e_r(\hat{A}_{i\_aui})$ and $e_r(\hat{B}_{i\_aui})$, which would increase along with the increase of monitoring periods $N_T$, and therefore the variance of $e_r(\hat{A}_{u\_aui})$, $e_r(\hat{B}_{u\_aui})$, $e_r(\hat{A}_{i\_aui})$ and $e_r(\hat{B}_{i\_aui})$ are reduced along with increasing of $N_T$ according to (11) and (13). As a result, $\hat{A}_{u\_aui}$, $\hat{B}_{u\_aui}$, $\hat{A}_{i\_aui}$ and $\hat{B}_{i\_aui}$ would be close to $A_{u\_aui}$, $B_{u\_aui}$, $A_{i\_aui}$ and $B_{i\_aui}$, respectively, along with the increase of $N_T$, and therefore the impact of noise can be relieved during the accumulation process in the proposed capacitor monitoring strategy.

### *B. Selection of Monitoring Periods $N_T$*

According to (23) and (24), the monitoring period $N_T$ is important in the proposed capacitance monitoring strategy, which would affect the effect of noise immunity. Fig. 7(a) shows the average error of the proposed method with active power of 0.8 p.u. under various $N_T$ and various SNR of the measurements, which are derived from the simulation in case I of Section V. Fig. 7(b) shows the average error with SNR=30 dB under various $N_T$ and various active power. It can be observed that the average error of the proposed strategy would decrease along with the increase of $N_T$. When $N_T$ is greater than 50, the increase of $N_T$ would not contribute much to the decrease of the capacitance monitoring error. Consequently, to make a tradeoff between the accuracy and time consumption, $N_T$ can be selected as 50 for the simulated system in Section V, which takes about one second for capacitance monitoring for each SM. For the MMC with 6 SMs per arm in the simulation studies in Section V, it requires about 36 s to complete capacitance monitoring once. Since the capacitor aging is a long-time effect [27], the variation of capacitance in a monitoring period can be neglected, which would not affect the accuracy of capacitance monitoring.

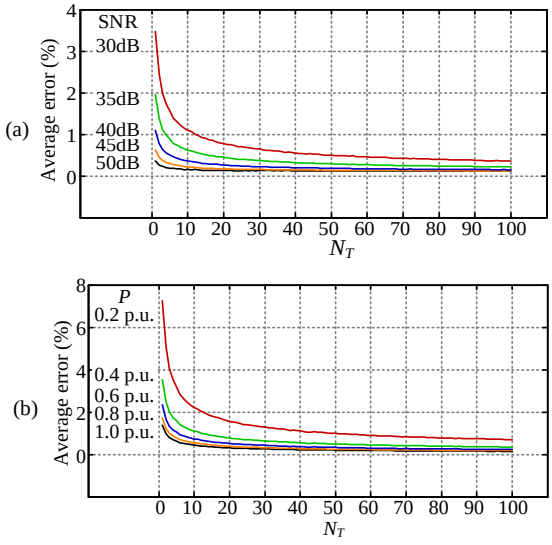


Fig. 7. Average error of the estimated capacitance. (a) $P$=0.8 p.u. under various $N_T$ and various SNRs of measured capacitor voltage and arm current. (b) SNR=30 dB under various $N_T$ and various active power.

This article has been accepted for publication in a future issue of this journal, but has not been fully edited. Content may change prior to final publication. Citation information: DOI 10.1109/TIE.2020.3014572, IEEE Transactions on Industrial Electronics

### C. Comparison of Capacitance Monitoring Methods

Table I shows a comparison of the proposed monitoring method and existing methods [15], [17], [24], [27]. The proposed capacitance monitoring strategy only requires capacitor voltage, arm current and reference, but not precise SM switching function. As a result, the proposed strategy can be directly implemented in the DSP controller with a simple algorithm. However, the methods in [15], [17] and [24] require precise SM switching function, which requires the DSP to receive precise SM switching states from FPGA. They bring the difficulty for the DSP to have such a high sampling speed to receive precise SM switching states from FPGA and handle such a large calculation amount.

The average error of capacitance monitoring with the proposed method and those methods in [15], [17], [24] and [27] under various SNRs of sampled capacitor voltage and arm current are shown in Fig. 8, which are derived from the simulated system in case I of Section V. It can be observed that the capacitance estimation errors in [24] and [27] are obviously increased along with the decrease of SNR, while the capacitance estimation errors in [15], [17] and the proposed method are nearly not affected by the SNR because the proposed method and the methods in [15], [17] are highly immune to noise, which greatly reduce the demands on the quality of sensors.

In comparison with other methods, the proposed method is more adaptive and has no effect on the performance of the MMC. However, the method in [15] requires to inject the ac current into the circulating current and the method in [17] is only suitable for the MMCs without CCSC, which both increase the arm current and power losses. The method in [24] requires the monitored SM and the reference SM have the same switching function, which affects the capacitor voltage balancing control. The method in [27] requires the monitored SM to be bypassed and discharged through the bleeding resistor, and other SMs are required to be operated with increased capacitor voltage.

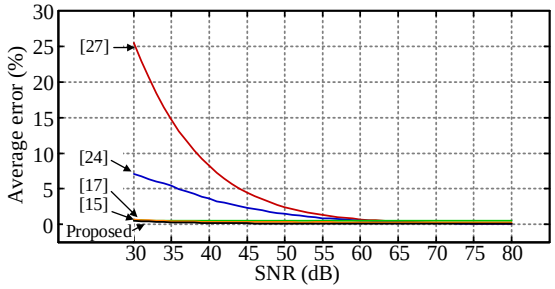


Fig. 8. Average error of the capacitance monitoring with different methods under various SNRs of measured capacitor voltage and arm current.

TABLE I
Comparison of the state-of-art capacitance monitoring methods for MMCs

| Method | Implementation | Noise immunity | Effects on Performance |
|---|---|---|---|
| Ref. [27] | Simple | No | Yes |
| Ref. [24] | Difficult (require switching state) | No | Yes |
| Ref. [17] | Difficult (require switching state) | Yes | Yes |
| Ref. [15] | Difficult (require switching state) | Yes | Yes |
| Proposed method | Simple | Yes | No |

Based on the above comparisons, the proposed capacitance monitoring method would be a better candidate for the PSC-PWM based MMC with the advantages of simple implementation, noise immunity and no effect on the control performance.

## V. Simulation Studies

To verify the proposed capacitance monitoring strategy, a three-phase MMC system, as shown in Fig. 9, is simulated with PSCAD/EMTDC. In the simulation, the capacitors in upper arm of phase A are monitored. The capacitance $C_{au5}$ and $C_{au6}$ drops as $C_{au5}$=7.2 mF, $C_{au6}$=6.4 mF. The active power $P$ and reactive power $Q$ are 4 MW (0.8 p.u.) and 0 MVar, respectively. The system parameters are shown in Table II.

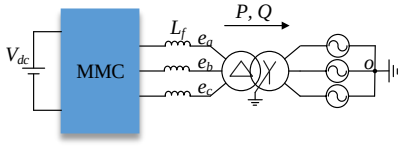


Fig. 9. Diagram of the simulated MMC system.

TABLE II
System Parameters for Simulation

| Parameter | Value |
|---|---|
| Rated power | 5 MVA |
| DC link voltage $V_{dc}$ | 6 kV |
| Grid line-to-line voltage | 33 kV |
| Rated frequency $f_0$ | 50 Hz |
| Transformer voltage rating | 3 kV/33 kV |
| Transformer leakage reactance | 10% |
| Number of SM per arm $N$ | 6 |
| Rated SM capacitance | 8 mF |
| Arm inductance $L_s$ | 3 mH |
| Filter inductance $L_f$ | 1 mH |
| Carrier frequency | 1 kHz |
| Sampling step $T_s$ | 100 us |
| SNR of system | 30 dB |
| $N_T$ | 50 |

### A. Case I: Monitoring under P=0.8 p.u. & Q=0

Figs. 10 (a) and (b) show the ideal capacitor voltages without noise and the sampled capacitor voltages with noise, respectively. Figs. 11 (c) and (d) show the ideal upper arm current without noise and the sampled upper arm current with noise. It can be observed that due to the large dc components in the capacitor voltages, the ripple components are more seriously affected by the sensor noise than the arm current. Besides, the voltage ripple of the SM with reduced capacitance is greater than the SM with rated capacitance.

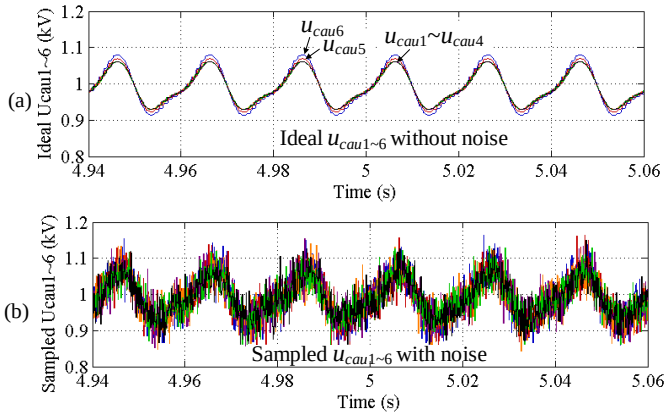

This article has been accepted for publication in a future issue of this journal, but has not been fully edited. Content may change prior to final publication. Citation information: DOI 10.1109/TIE.2020.3014572, IEEE Transactions on Industrial Electronics

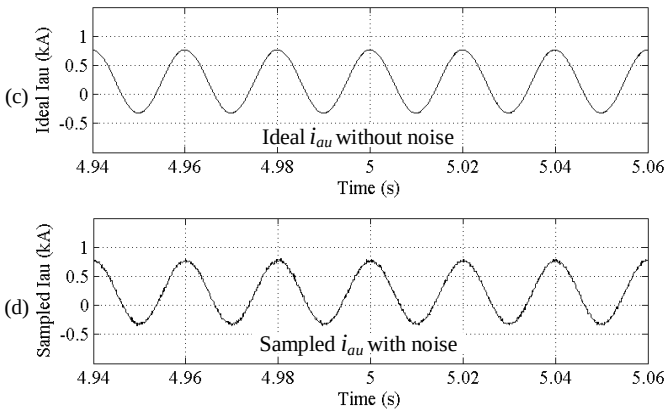


Fig. 10. Simulation results under rated condition. (a) Ideal $u_{cau1}$~$u_{cau6}$. (b) Sampled $u_{cau1}$~$u_{cau6}$ with 30 dB noise. (c) Ideal $i_{au}$. (d) Sampled $i_{au}$ with 30 dB noise.

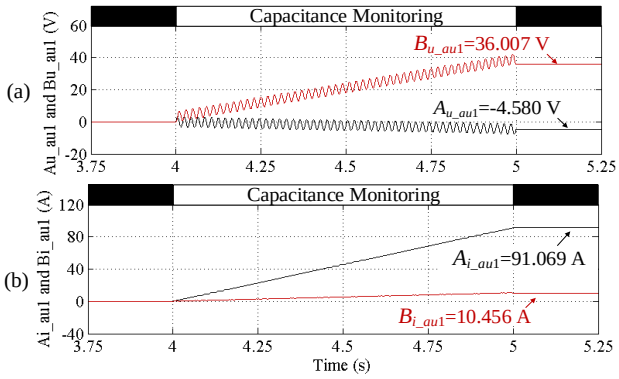


Fig. 11. Simulation result under rated condition. (a) $A_{u\_au1}$ and $B_{u\_au1}$ (b) $A_{i\_au1}$ and $B_{i\_au1}$.

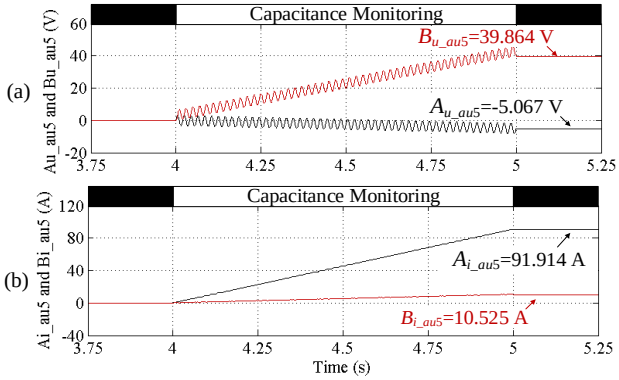


Fig. 12. Simulation results under rated condition. (a) $A_{u\_au5}$ and $B_{u\_au5}$ (b) $A_{i\_au5}$ and $B_{i\_au5}$.

The performance of the proposed method for SM 1 with rated capacitance is shown in Fig. 11. Fig. 11(a) shows the integral process of $A_{u\_au1}$ and $B_{u\_au1}$. Fig. 11(b) shows the integral process of $A_{i\_au1}$ and $B_{i\_au1}$. The capacitor monitoring begins at t=4 s. Then, the amplitude of $A_{u\_au1}$, $B_{u\_au1}$, $A_{i\_au1}$ and $B_{i\_au1}$ increase along with execution of the capacitance monitoring process. At t=5 s, the capacitance monitoring ends and $C_{au1}$ is estimated as 8.039 mF with (12), (14) and (15).

The performance of the proposed method for SM 5 with reduced capacitance is shown in Fig. 12. Fig. 12(a) shows the integral process of $A_{u\_au5}$ and $B_{u\_au5}$. Fig. 12(b) shows the integral process of $A_{i\_au5}$ and $B_{i\_au5}$. The capacitance monitoring begins at t=4 s. Then, the amplitude of $A_{u\_au5}$, $B_{u\_au5}$, $A_{i\_au5}$ and $B_{i\_au5}$ increase along with the execution of the capacitance monitoring process. In comparison with the results of SM 1, as shown in Fig. 11, the amplitudes of $A_{u\_au5}$ and $B_{u\_au5}$ are respectively greater than the $A_{u\_au1}$ and $B_{u\_au1}$, because the voltage ripple of SM 5 is greater than the voltage ripple of SM 1 due to the reduced capacitance, as shown in Fig. 10(a). At t=5 s, the capacitor monitoring ends and $C_{au5}$ of SM 5 is estimated as 7.250 mF.

The SMs in upper arm of phase A are estimated one by one by the proposed capacitance monitoring strategy. The estimated capacitance $C_{au1}$~$C_{au6}$ are shown in Fig. 13(a) and the errors of the estimation are shown in Fig. 13(b), where the maximum error is 0.69%.

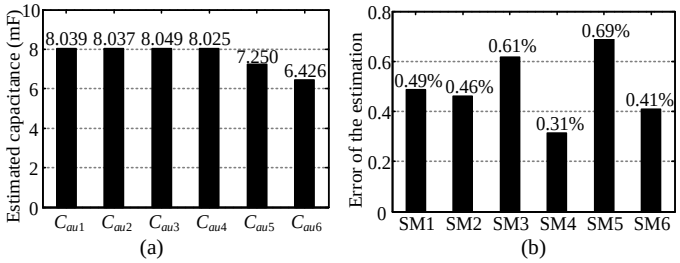


Fig. 13. Simulation results under rated condition. (a) Estimated capacitance $C_{au1}$~$C_{au6}$. (b) Errors of estimated capacitance.

### *B. Case II: Monitoring with Low Switching Frequency*

Fig. 14 shows the performance of the MMC with low switching frequency, where the SM switching frequency is 250 Hz. Figs. 14(a) and (b) show the ideal capacitor voltages without noise and the sampled capacitor voltages with noise, respectively. Figs. 14 (c) and (d) show the ideal upper arm current without noise and the sampled upper arm current with noise.

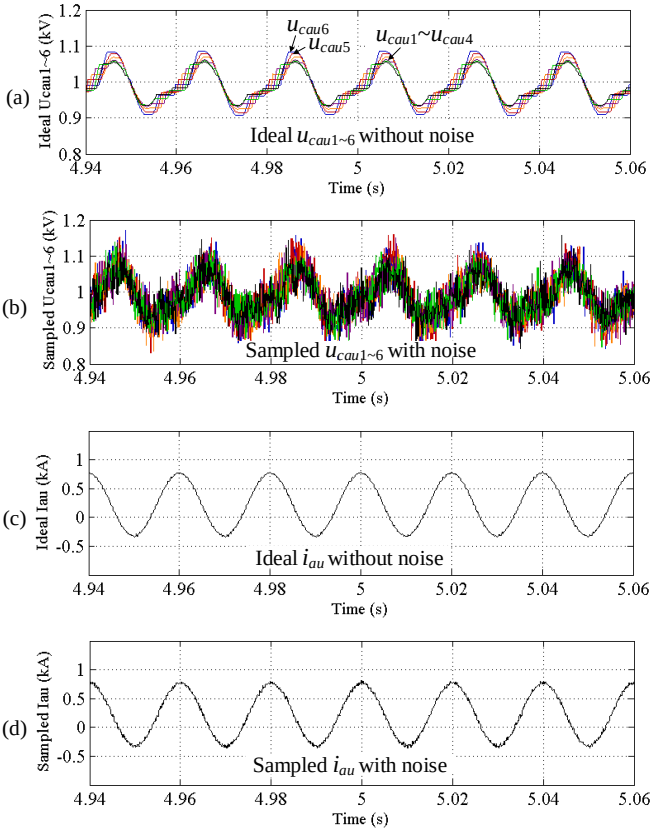


Fig. 14. Simulation results with low switching frequency. (a) Ideal $u_{cau1}$~$u_{cau6}$. (b) Sampled $u_{cau1}$~$u_{cau6}$ with 30 dB noise. (c) Ideal $i_{au}$. (d) Sampled $i_{au}$ with 30 dB noise.

This article has been accepted for publication in a future issue of this journal, but has not been fully edited. Content may change prior to final publication. Citation information: DOI 10.1109/TIE.2020.3014572, IEEE Transactions on Industrial Electronics

The estimated capacitance $C_{au1}$~$C_{au6}$ in upper arm of phase A are shown in Fig. 15(a) and the errors of the estimation are shown in Fig. 15(b), where the maximum error is 0.58%. In comparison with the results in case I, the estimation error is not increased due to the reduced switching frequency.

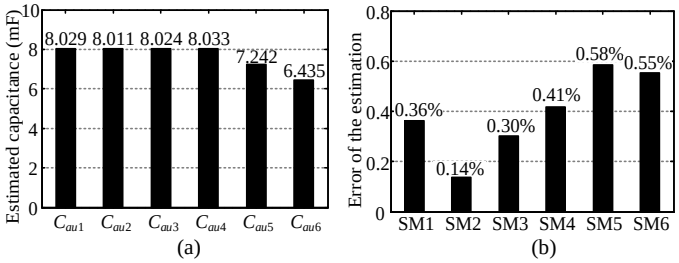


Fig. 15. Simulation results with low switching frequency. (a) Estimated capacitance $C_{au1}$~$C_{au6}$. (b) Errors of estimated capacitance.

Fig. 16 shows the average error of the proposed capacitance monitoring method under various switching frequencies and various SNRs. It can be observed that the average error almost remains constant under various switching frequencies and the average error is decreased along with the increase of the SNR.

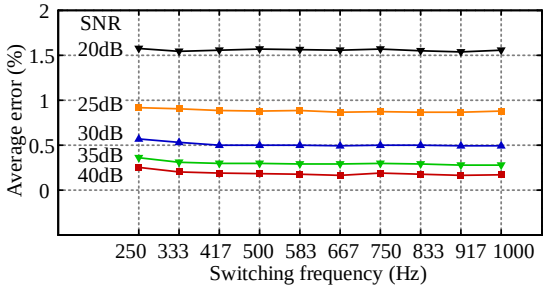


Fig. 16. Average error of the proposed method under various switching frequencies and various SNRs.

## VI. Experimental Studies

A three-phase MMC is built in laboratory to confirm the proposed strategy. A photo of experimental setup is shown in Fig. 17. A dc source SGA600/10 is adopted to support the dc link voltage and a voltage regulator is adopted to support the ac voltage. The output current control [39], CCSC [32] and capacitor voltage balancing control [31] are implemented in the DSP TMS320F28346, while the FPGA XC6SLX16 is adopted to achieve the PSC-PWM scheme and generate the driver signals. Then, the pulse signals are transferred to each SM via optical fiber. The voltage sensors LEM LV25-P [40] are equipped to convert the capacitor voltage to voltage signal while the current sensors LEM LA55-P [41] are equipped to convert the arm current to voltage signal. And the voltage signals are sampled by the analog-digital converter (ADC). The system parameters are listed in TABLE III.

To verify the proposed capacitance monitoring strategy, the small capacitances $C_{au3}$ and $C_{au4}$ are adopted, where manufacture parameters are given as 1.88 mF and 1.41 mF, respectively. The proposed scheme is implemented in the DSP controller, and the internal signals $A_{u\_aui}$, $B_{u\_aui}$, $A_{i\_aui}$ and $B_{i\_aui}$ are output by the digital-analog converter (DAC) and recorded by an oscilloscope, while the capacitance monitoring results are directly transferred from the DSP controller to the host computer through Transmission Control Protocol (TCP) based Ethernet.

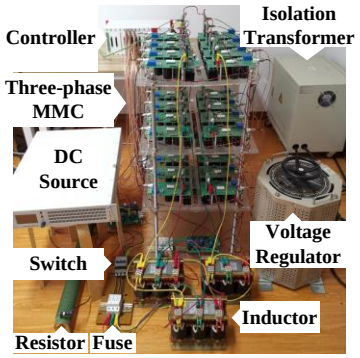


Fig. 17. Photo of the experimental MMC system.

TABLE III
Parameters for Three-Phase MMC Experimental System

| Parameter | Value |
|---|---|
| Rated Power | 1 kW |
| DC link voltage $V_{dc}$ | 200 V |
| AC line-to-line voltage | 100 V |
| Rated frequency $f_0$ | 50 Hz |
| Number of SM per arm $N$ | 4 |
| Rated SM capacitance | 2.35 mF |
| Arm inductance $L_s$ | 3 mH |
| Filter inductance $L_f$ | 3 mH |
| Carrier frequency | 1 kHz |
| Sampling step $T_s$ | 100 us |

### A. Case I: Monitoring under P=0.8 p.u. & Q=0

Fig. 18 shows the performance of the MMC, where the power with active power of 0.8 p.u. and reactive power of 0 p.u. are transferred from dc side to ac side. Fig. 18(a) shows the capacitor voltages $u_{cau1}$~$u_{cau4}$ in the upper arm of phase A, which are obtained by voltage probes with 50 kHz low-pass filter. Fig. 18(b) shows the output voltages of capacitor voltage sensors for $u_{cau1}$~$u_{cau4}$ by the voltage probes with full bandwidth. The ripples of $u_{cau3}$ and $u_{cau4}$ are greater than those of $u_{cau1}$ and $u_{cau2}$ due to the reduced $C_{au3}$ and $C_{au4}$. Fig. 18(c) shows the arm currents $i_{au}$ and $i_{al}$, which are obtained from the arm circuit by the current probes with a 50 kHz low-pass filter. Fig. 18(d) shows the output voltages of current sensors for $i_{au}$ and $i_{al}$ by the voltage probes with full bandwidth. It can be observed that the measured capacitor voltages and arm currents through sensors are affected by noise. Owing to that the capacitor voltage ripple accounts for a small part in capacitor voltage, the capacitor voltage ripple measured from voltage sensors are more seriously affected by the noise than the arm current.

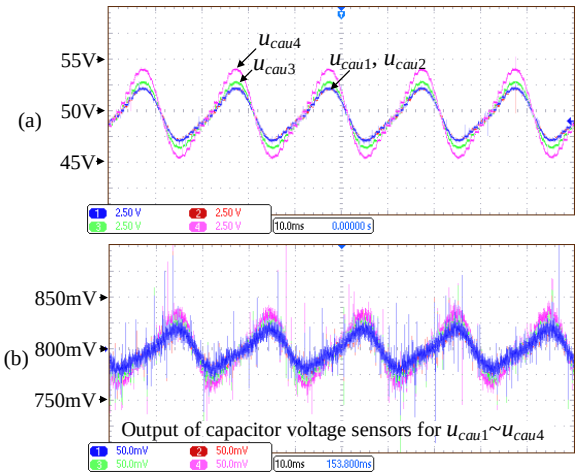

This article has been accepted for publication in a future issue of this journal, but has not been fully edited. Content may change prior to final publication. Citation information: DOI 10.1109/TIE.2020.3014572, IEEE Transactions on Industrial Electronics

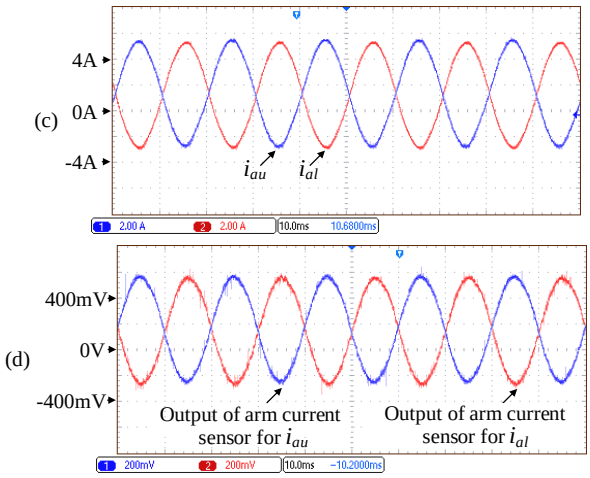


Fig. 18. Experimental results under rated condition. (a) $u_{cau1}$~$u_{cau4}$. (b) Output of capacitor voltage sensors for $u_{cau1}$~$u_{cau4}$. (c) $i_{au}$ and $i_{al}$. (d) Output of current sensors for $i_{au}$ and $i_{al}$. Time base is 10 ms/div.

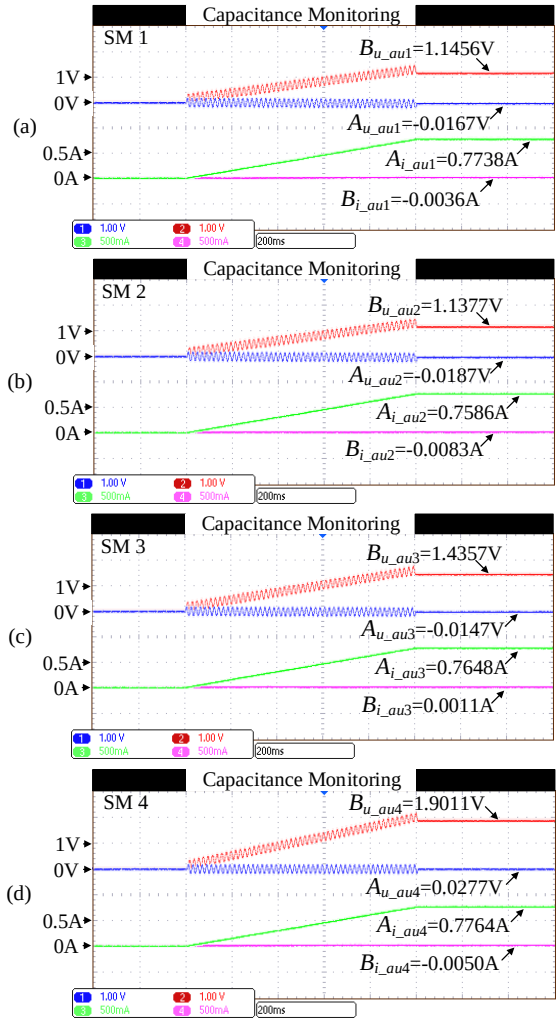


Fig. 19. Experimental results under rated condition. (a) $A_{u\_au1}$, $B_{u\_au1}$, $A_{i\_au1}$ and $B_{i\_au1}$ for SM 1. (b) $A_{u\_au2}$, $B_{u\_au2}$, $A_{i\_au2}$ and $B_{i\_au2}$ for SM 2. (c) $A_{u\_au3}$, $B_{u\_au3}$, $A_{i\_au3}$ and $B_{i\_au3}$ for SM 3. (d) $A_{u\_au4}$, $B_{u\_au4}$, $A_{i\_au4}$ and $B_{i\_au4}$ for SM 4. Time base is 200 ms/div.

The performance under the proposed capacitance monitoring strategy is shown in Fig. 19. Fig. 19(a) shows the integral process of $A_{u\_au1}$, $B_{u\_au1}$, $A_{i\_au1}$ and $B_{i\_au1}$ for SM 1, where the amplitude of $A_{u\_au1}$, $B_{u\_au1}$, $A_{i\_au1}$ and $B_{i\_au1}$ increase along with execution of the capacitance monitoring process. Afterwards, $C_{au1}$ is estimated to be 2.150 mF. Figs. 19 (b), (c) and (d) show the integral process for SM 2, SM 3 and SM 4, respectively.

Fig. 20(a) shows the estimated capacitance with proposed scheme and the measured capacitance using the UNI-T UT612 LCR meter. Fig. 20(b) shows the relative errors between estimated capacitance and the measured capacitance, where the maximum error is 0.59%.

Fig. 21 shows the estimated capacitance of SM 1 under various active power from 0.2 p.u. to 1.0 p.u., where the proposed capacitance monitoring strategy is conducted forty times for each case. It can be observed that along with the increase of the active power, the proposed strategy shows reduced errors. In most of the cases, the error of the estimated capacitance is less than 1%.

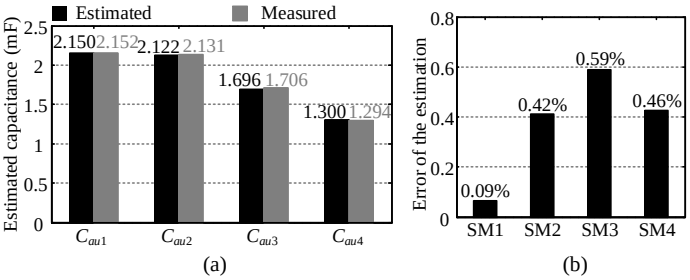


Fig. 20. Experimental results under rated condition. (a) Estimated capacitance $C_{au1}$~$C_{au4}$. (b) Errors of estimated capacitance.

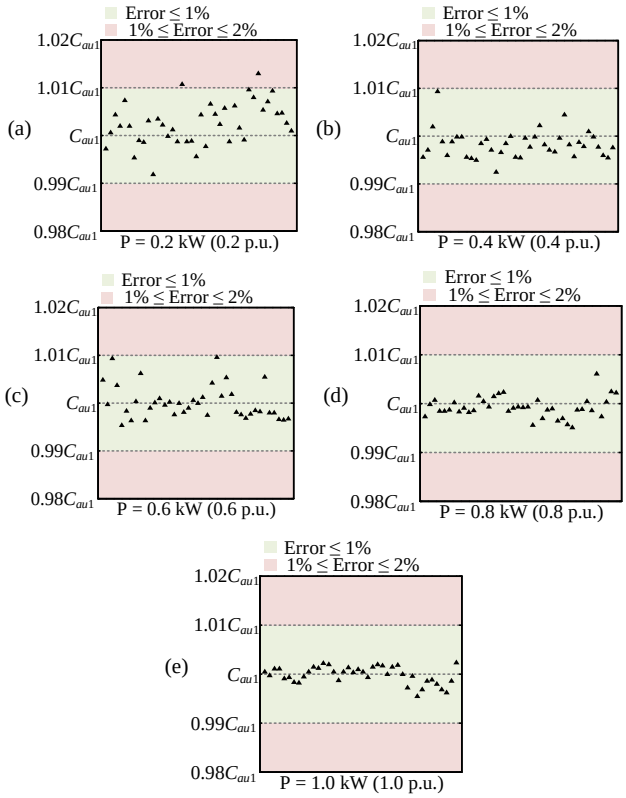


Fig. 21. Estimated capacitance of SM 1 under various active power operation. (a) 0.2 p.u. (b) 0.4 p.u. (c) 0.6 p.u. (d) 0.8 p.u. (e) 1.0 p.u.

### *B. Case II: Monitoring with Low Switching Frequency*

Fig. 22 shows the performance of the MMC, where the switching frequency for each SM is 390 Hz. Fig. 22(a) shows the capacitor voltages $u_{cau1}$~$u_{cau4}$ in the upper arm of phase A. Fig. 22(b) shows the output voltages of the capacitor voltage

This article has been accepted for publication in a future issue of this journal, but has not been fully edited. Content may change prior to final publication. Citation information: DOI 10.1109/TIE.2020.3014572, IEEE Transactions on Industrial Electronics

sensors for $u_{cau1}$~$u_{cau4}$. The ripples of $u_{cau3}$ and $u_{cau4}$ are greater than those of $u_{cau1}$ and $u_{cau2}$ due to the reduced $C_{au3}$ and $C_{au4}$. Fig. 22(c) shows the upper arm current $i_{au}$ and the lower arm current $i_{al}$. Fig. 22(d) shows the output voltages of current sensors for $i_{au}$ and $i_{al}$. The arm currents are slightly distorted due to the low switching frequency.

Fig. 23(a) shows the estimated capacitance with proposed scheme and the measured capacitance using the UNI-T UT612 LCR meter. Fig. 23(b) shows the relative errors between estimated capacitance and the measured capacitance, where the maximum error is 0.54%. In comparison with the results in case I, the estimation error is not increased due to the low switching frequency.

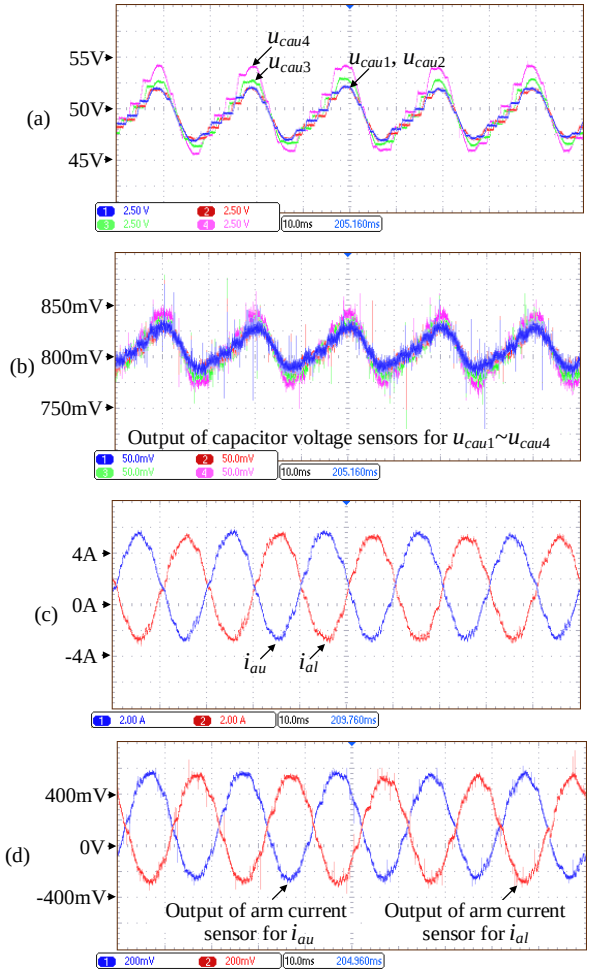


Fig. 22. Experimental results with low switching frequency. (a) $u_{cau1}$~$u_{cau4}$. (b) Output of capacitor voltage sensors for $u_{cau1}$~$u_{cau4}$. (c) $i_{au}$ and $i_{al}$. (d) Output of current sensors for $i_{au}$ and $i_{al}$. Time base is 10 ms/div.

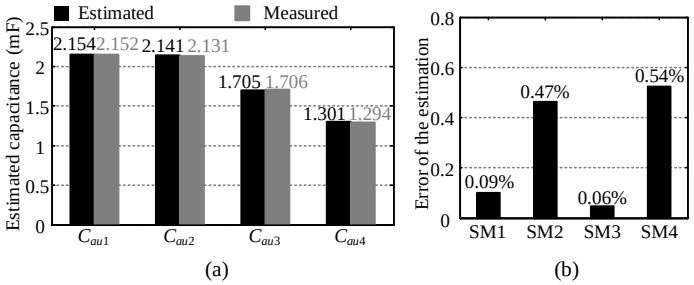


Fig. 23. Experimental results with low switching frequency. (a) Estimated capacitance $C_{au1}$~$C_{au4}$. (b) Errors of estimated capacitance.

### C. Case III: Monitoring with Various Modulation Indexes

To test the performance of the proposed method under various modulation indexes, the ac-side voltage is changed so that the MMC can work with various modulation indexes. The estimated capacitance and relative error for SM 2 with proposed method under various modulation indexes are listed in TABLE IV. It can be observed that the error of the estimation is lower than 1% when the modulation index is above 0.4. Normally, the modulation index is rarely low as 0.4 during normal operation in practical application.

TABLE IV
Experimental Results for SM 2 under Various Modulation Index

| Modulation Index | Estimated Capacitance (mF) | Errors (%) |
|---|---|---|
| 0.2 | 2.159 | 1.31 |
| 0.4 | 2.144 | 0.61 |
| 0.6 | 2.143 | 0.56 |
| 0.8 | 2.138 | 0.33 |

### D. Case IV: Monitoring with Different Power Factors

To test the performance of the proposed method under different power factors, the apparent power of the MMC is kept at 0.8 p.u. and the power factor varies from 1 to 0. The estimated capacitances and relative errors for SM 2 under various power factors are listed in TABLE V. It can be observed that the accuracy of the estimated capacitance is almost not affected by the power factors.

TABLE V
Experimental Results for SM 2 under Various Power Factors

| Power Factor | Estimated Capacitance (mF) | Errors (%) |
|---|---|---|
| 1.0 | 2.139 | 0.38 |
| 0.8 | 2.145 | 0.66 |
| 0.6 | 2.138 | 0.33 |
| 0.4 | 2.134 | 0.14 |
| 0.2 | 2.127 | 0.19 |
| 0 | 2.136 | 0.23 |

### E. Case V: Monitoring with Different Load Frequency

To test the performance of the proposed method under different load frequency, the MMC with filter inductor and resistor load of 10 Ω is adopted and the load frequency is 25 Hz.

Fig. 24 shows the integral process of $A_{u\_au1}$, $B_{u\_au1}$, $A_{i\_au1}$ and $B_{i\_au1}$ for SM 1 and $C_{au1}$ is estimated to be 2.153 mF. Because of the reduced load frequency, the monitoring time is prolonged to about 2 s in comparison with the case I.

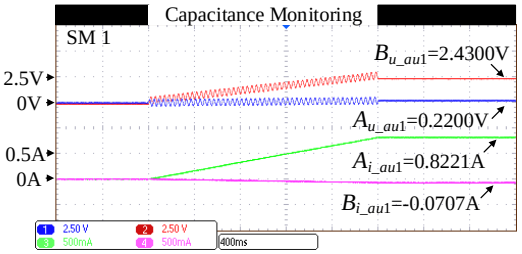


Fig. 24. Experimental results of $A_{u\_au1}$, $B_{u\_au1}$, $A_{i\_au1}$ and $B_{i\_au1}$ for SM 1 with load frequency of 25 Hz. Time base is 400 ms/div.

Fig. 25(a) shows the estimated capacitance with proposed scheme and the measured capacitance using the UNI-T UT612 LCR meter. Fig. 25(b) shows the relative errors between estimated capacitance and the measured capacitance, where the maximum error is 0.54%.

This article has been accepted for publication in a future issue of this journal, but has not been fully edited. Content may change prior to final publication. Citation information: DOI 10.1109/TIE.2020.3014572, IEEE Transactions on Industrial Electronics

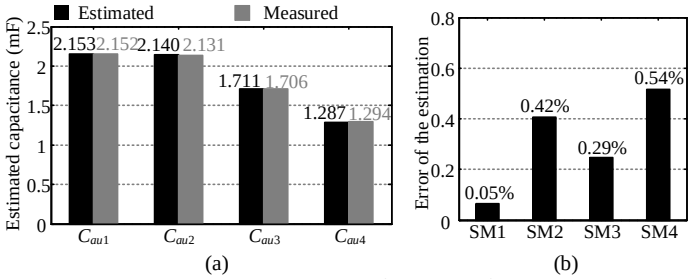


Fig. 25. Experimental results with load frequency of 25 Hz. (a) Estimated capacitance $C_{au1}$~$C_{au4}$. (b) Errors of estimated capacitance.

### F. Case VI: Monitoring with Arm Inductor Mismatch

To test the performance of the proposed capacitor monitoring method under arm inductor mismatch, the arm inductor in the upper arm of phase A is 1.5 mH and the arm inductors in other arms are 3 mH.

Fig. 26(a) shows the estimated capacitance with proposed scheme and the measured capacitance using the UNI-T UT612 LCR meter. Fig. 26(b) shows the relative errors between estimated capacitance and the measured capacitance, where the maximum error is 0.7%.

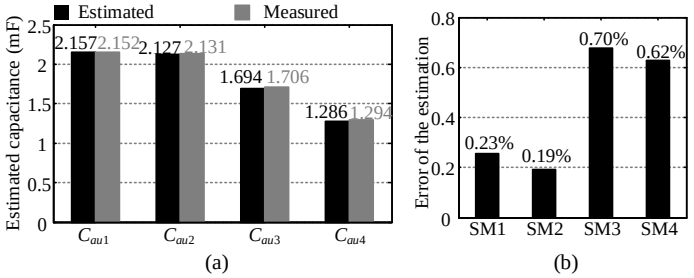


Fig. 26. Experimental results with arm inductor mismatch. (a) Estimated capacitance $C_{au1}$~$C_{au4}$. (b) Errors of estimated capacitance.

### G. Case VII: Monitoring with Increased Capacitance

To test the performance of the proposed capacitance method with increased capacitance, the SM 1 with larger capacitance is adopted and the capacitance is measured as 2.616 mF using the UNI-T UT612 LCR meter.

Fig. 27 shows the integral process of $A_{u\_au1}$, $B_{u\_au1}$, $A_{i\_au1}$ and $B_{i\_au1}$ for SM 1, where the amplitude of $A_{u\_au1}$, $B_{u\_au1}$, $A_{i\_au1}$ and $B_{i\_au1}$ increase along with execution of the capacitance monitoring process. Afterwards, $C_{au1}$ is estimated to be 2.598 mF and the estimation error is 0.69%.

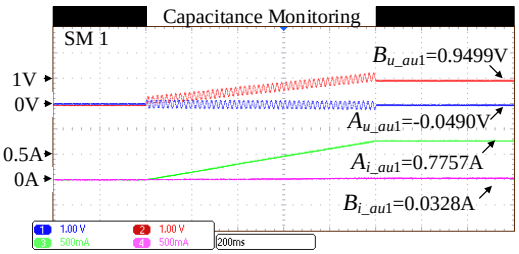


Fig. 27. Experimental results of $A_{u\_au1}$, $B_{u\_au1}$, $A_{i\_au1}$ and $B_{i\_au1}$ for SM 1 with increased capacitance. Time base is 200 ms/div.

### H. Temperature Effect on Capacitance

The capacitance of the electrolytic capacitor also depends on the capacitor temperature. The capacitance increases along with the increase of the temperature due to the changing properties of the relative permittivity of the capacitor's dielectric material [42]. In order to determine the relationship between capacitance and temperature of the capacitor, the temperature chamber is used to keep the capacitor temperature constant and the capacitance is measured by LCR meter. Fig. 28 shows the photo of the experimental system.

Fig. 29 shows the measured capacitance of five capacitor samples under various temperature from 25 °C to 85 °C. The measured results of five samples are fitted with linear model [43], respectively, as plotted in Fig. 29. The corresponding coefficient of determination $R^2$ of fit is adopted to evaluate the effectiveness of the linear fit. In Fig. 29, the minimum $R^2$ of the fitting results is 99.62%, which proves that the relationship between capacitance and temperature can be fitted well by the linear model. The average value (dash line) of the five fit results is also plotted in Fig. 29 and the slope of the average value is 1.73 uF/°C. With the capacitance estimated by the proposed capacitance monitoring method and the capacitor temperature, the capacitance at 25 °C can be obtained based on the slope of the average value of these fit results. And then, the capacitor is judged to be failed if its capacitance at 25 °C is less than the threshold value.

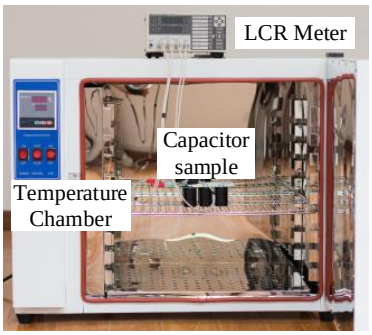


Fig. 28. Photo of the experimental system.

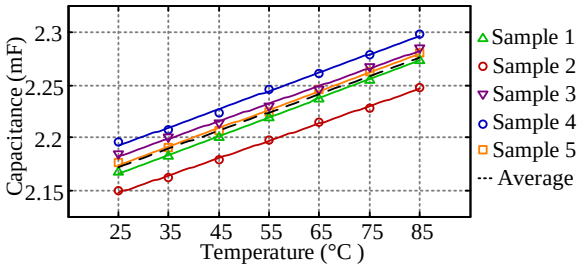


Fig. 29. The measured capacitance of five samples under various temperatures and their fitting results.

## VII. Conclusion

This paper presents a submodule capacitance monitoring strategy for PSC-PWM based MMC, where the fundamental frequency components of the SM capacitor voltage and current are extracted to estimate the SM capacitance based on the reference, but do not need the precise switching states. The proposed scheme not only simplifies the implementation and calculations, but also avoids heavy communication burden between DSP and FPGA as well as extra control or any effect on the control performance. In addition, the impact of noise is also analyzed, where the proposed monitoring strategy can eliminate noise impact from sensors and increase accuracy. Simulation and experimental studies are also implemented, and the results confirm the effectiveness of the proposed strategy.

## REFERENCES


[1] C. Wang, K. Wang, Z. Zheng, B. Yang, K. Sun and Y. Li, "Analysis and Control of Three-Phase Modular Multilevel Converters Under the Single Arm Fault Condition," *IEEE Trans. Power Electron.*, vol. 34, no. 9, pp. 8293-8298, Sept. 2019.

[2] F. Deng *et al*., "Power Losses Control for Modular Multilevel Converters Under Capacitor Deterioration," *IEEE J. Emerg. Sel. Topics Power Electron*., accepted, 2019.

[3] C. Liu *et al*., "Fault Localization Strategy for Modular Multilevel Converters Under Submodule Lower Switch Open-Circuit Fault," *IEEE Trans. Power Electron.*, vol. 35, no. 5, pp. 5190-5204, May 2020.

[4] S. Debnath, J. Qin, B. Bahrani, M. Saeedifard and P. Barbosa, "Operation, Control, and Applications of the Modular Multilevel Converter: A Review," *IEEE Trans. Power Electron.*, vol. 30, no. 1, pp. 37-53, Jan. 2015.

[5] J. Lee, J. Jung and S. Sul, "Balancing of Submodule Capacitor Voltage of Hybrid Modular Multilevel Converter Under DC-Bus Voltage Variation of HVDC System," *IEEE Trans. Power Electron.*, vol. 34, no. 11, pp. 10458-10470, Nov. 2019.

[6] G. Guo *et al*., "HB and FB MMC Based Onshore Converter in Series-Connected Offshore Wind Farm," *IEEE Trans. Power Electron.*, vol. 35, no. 3, pp. 2646-2658, March 2020.

[7] Z. Li, R. Lizana F., Z. Yu, S. Sha, A. V. Peterchev and S. M. Goetz, "A Modular Multilevel Series/Parallel Converter for a Wide Frequency Range Operation," *IEEE Trans. Power Electron.*, vol. 34, no. 10, pp. 9854-9865, Oct. 2019.

[8] H. Soliman, H. Wang and F. Blaabjerg, "A Review of the Condition Monitoring of Capacitors in Power Electronic Converters," *IEEE Trans. Ind. Appl*., vol. 52, no. 6, pp. 4976-4989, Nov.-Dec. 2016.

[9] Y. Chen, H. Wu, M. Chou and K. Lee, "Online Failure Prediction of the Electrolytic Capacitor for LC Filter of Switching-Mode Power Converters," *IEEE Trans. Ind. Electron.*, vol. 55, no. 1, pp. 400-406, Jan. 2008.

[10] Y. Wang, C. Hu, R. Ding, L. Xu, C. Fu and E. Yang, "A Nearest Level PWM Method for the MMC in DC Distribution Grids," *IEEE Trans. Power Electron.*, vol. 33, no. 11, pp. 9209-9218, Nov. 2018.

[11] S. Zhou, B. Li, M. Guan, X. Zhang, Z. Xu and D. Xu, "Capacitance Reduction of the Hybrid Modular Multilevel Converter by Decreasing Average Capacitor Voltage in Variable-Speed Drives," *IEEE Trans. Power Electron.*, vol. 34, no. 2, pp. 1580-1594, Feb. 2019.

[12] Y. S. Kumar and G. Poddar, "Medium-Voltage Vector Control Induction Motor Drive at Zero Frequency Using Modular Multilevel Converter," *IEEE Trans. Ind. Electron.*, vol. 65, no. 1, pp. 125-132, Jan. 2018.

[13] M. A. Vogelsberger, T. Wiesinger and H. Ertl, "Life-Cycle Monitoring and Voltage-Managing Unit for DC-Link Electrolytic Capacitors in PWM Converters," *IEEE Trans. Power Electron.*, vol. 26, no. 2, pp. 493-503, Feb. 2011.

[14] H. Wang and F. Blaabjerg, "Reliability of Capacitors for DC-Link Applications in Power Electronic Converters—An Overview," *IEEE Trans. Ind. Appl.*, vol. 50, no. 5, pp. 3569-3578, Sept.-Oct. 2014.

[15] Y. Jo, T. H. Nguyen and D. Lee, "Condition monitoring of submodule capacitors in modular multilevel converters," in *Proc. ECCE* 2014, pp. 2121-2126.

[16] D. Ronanki and S. S. Williamson, "Quasi-Online Low-Frequency Impedance Monitoring Scheme for Submodule Capacitors in Modular Multilevel Converters," in *IEEE Applied Power Electron. Conf. and Expo*., 2019, pp. 83-90.

[17] D. Ronanki and S. S. Williamson, "Failure Prediction of Submodule Capacitors in Modular Multilevel Converter by Monitoring the Intrinsic Capacitor Voltage Fluctuations," *IEEE Trans. Ind. Electron.*, vol. 67, no. 4, pp. 2585-2594, April 2020.

[18] D. Ronanki and S. S. Williamson, "Capacitance Estimation in Modular Multilevel Converters under Nearest Level Modulation Scheme," in *Proc. IEEE 28th Int. Symp. Ind. Electron.*, 2019, pp. 2371-2376.

[19] D. Ronanki and S. S. Williamson, "Health Monitoring Scheme for Submodule Capacitors in Modular Multilevel Converter Utilizing Capacitor Voltage Fluctuations," in *Proc. IECON*, 2018, pp. 2068-2073.

[20] O. Abushafa, S. Gadoue, M. Dahidah and D. Atkinson, "A new scheme for monitoring submodule capacitance in modular multilevel converter," in *Proc. PEMD*, 2016, pp. 1-6.

[21] C. Zhang, W. Zhang, S. Ethni, M. Dahidah, V. Pickert and H. Khalfalla, "Online Condition Monitoring of Sub-module Capacitors in MMC Enabled by Reduced Switching Frequency Sorting Scheme," in *Proc. 10th Int. Renewable Energy Congress*, 2019, pp. 1-6.

[22] N. Yu, S. Shao, X. Wu, J. Zhang and H. Chen, "Application of Tunnel Magnetoresistance to Health Monitoring of Modular Multilevel Converter Submodules," in *IEEE Int. Power Electron. App. Conf. Expo*., 2018, pp. 1-5.

[23] F. Deng, D. Liu, Y. Wang, Z. Chen, M. Cheng and Q. Wang, "Capacitor monitoring for modular multilevel converters," in *Proc. IECON* 2016, 2017, pp. 934-939.

[24] F. Deng, Q. Wang, D. Liu, Y. Wang, M. Cheng and Z. Chen, "Reference Submodule Based Capacitor Monitoring Strategy for Modular Multilevel Converters," *IEEE Trans. Power Electron.*, vol. 34, no. 5, pp. 4711-4721, May 2019.

[25] Z. Wang, Y. Zhang, H. Wang and F. Blaabjerg, "A Reference Submodule Based Capacitor Condition Monitoring Method for Modular Multilevel Converters," *IEEE Trans. Power Electron.*, vol. 35, no. 7, pp. 6691-6696, July 2020.

[26] F. Deng *et al*., "Capacitor ESR and C Monitoring in Modular Multilevel Converters," *IEEE Trans. Power Electron.*, vol. 35, no. 4, pp. 4063-4075, April 2020.

[27] H. Wang, H. Wang, Z. Wang, Y. Zhang, X. Pei and Y. Kang, "Condition Monitoring for Submodule Capacitors in Modular Multilevel Converters," *IEEE Trans. Power Electron.*, vol. 34, no. 11, pp. 10403-10407, Nov. 2019.

[28] Z. Wang, Y. Zhang, H. Wang and F. Blaabjerg, "Capacitor Condition Monitoring Based on the DC-Side Start-Up of Modular Multilevel Converters," *IEEE Trans. Power Electron.*, vol. 35, no. 6, pp. 5589-5593, June 2020.

[29] K. Wang, L. Jin, G. Li, Y. Deng and X. He, "Online Capacitance Estimation of Submodule Capacitors for Modular Multilevel Converter With Nearest Level Modulation," *IEEE Trans. Power Electron.*, vol. 35, no. 7, pp. 6678-6681, July 2020.

[30] M. Hagiwara and H. Akagi, "Control and Experiment of Pulsewidth-Modulated Modular Multilevel Converters," *IEEE Trans. Power Electron.*, vol. 24, no. 7, pp. 1737-1746, July 2009.

[31] B. Li, R. Yang, D. Xu, G. Wang, W. Wang and D. Xu, "Analysis of the Phase-Shifted Carrier Modulation for Modular Multilevel Converters," *IEEE Trans. Power Electron.*, vol. 30, no. 1, pp. 297-310, Jan. 2015.

[32] Q. Tu, Z. Xu and L. Xu, "Reduced Switching-Frequency Modulation and Circulating Current Suppression for Modular Multilevel Converters," *IEEE Trans. Power Del.*, vol. 26, no. 3, pp. 2009-2017, July 2011.

[33] F. Deng, C. Liu, Q. Wang, R. Zhu, X. Cai and Z. Chen, "A Currentless Submodule Individual Voltage Balancing Control for Modular Multilevel Converters," *IEEE Trans. Ind. Electron.*, accepted, 2019.

[34] P. Rodríguez, R. Teodorescu, I. Candela, A. V. Timbus, M. Liserre and F. Blaabjerg, "New positive-sequence voltage detector for grid synchronization of power converters under faulty grid conditions," in *Proc. PESC* 2006, pp. 1-7.

[35] X. Ai, H. Bao and Y. H. Song, "Novel method of error current compensation for Hall-effect-based high-accuracy current transformer," *IEEE Trans. Power Del*., vol. 20, no. 1, pp. 11-14, Jan. 2005.

[36] M. D. Islam, R. Razzaghi and B. Bahrani, "Arm-Sensorless Sub-Module Voltage Estimation and Balancing of Modular Multilevel Converters," *IEEE Trans. Power Del*., vol. 35, no. 2, pp. 957-967, April 2020.

[37] K. Jia, Z. Xuan, T. Feng, C. Wang, T. Bi and D. W. P. Thomas, "Transient High-Frequency Impedance Comparison-Based Protection for Flexible DC Distribution Systems," *IEEE Trans. Smart Grid*, vol. 11, no. 1, pp. 323-333, Jan. 2020.

[38] Q. Song, W. Yang, B. Zhao, J. Meng, S. Xu and Z. Zhu, "Low-capacitance modular multilevel converter operating with high capacitor voltage ripples," *IEEE Trans. Ind. Electron.*, vol. 66, no. 10, pp. 7456-7467, Oct. 2019.

[39] M. Saeedifard and R. Iravani, "Dynamic Performance of a Modular Multilevel Back-to-Back HVDC System," *IEEE Trans. Power Del.*, vol. 25, no. 4, pp. 2903-2912, Oct. 2010.

[40] "Voltage transducer LV25-P, datasheet, Doc. No. v19 2014." [Online]. Available: https://www.lem.com/en

[41] "Current transducer LA55-P, datasheet, Doc. No. v17 2018." [Online]. Available: https://www.lem.com/en

[42] F. Argall and A. Jonscher, "Dielectric properties of thin films of aluminium oxide and silicon oxide," *Thin Solid Films*, vol. 2, no. 3, pp. 185–210, 1968.

[43] J. Prymak, M. Randall, P. Blais, and B. Long, "Why that 47 uF capacitor drops to 37 uF, 30 uF, or lower," in *Proc. CARTS USA Conf.*, 2008, pp. 193–208.

**Chengkai Liu** was born in Fujian, China, in 1996. He received the B. Eng. degree in Electrical Engineering from Chien-Shiung WU College of Southeast University, Nanjing, China, in 2018. And he is currently working toward the Ph.D. degree with the School of Electrical Engineering, Southeast University.

His main research interests include multilevel converters and dc grids.

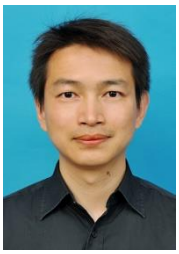

**Fujin Deng** (SM'19) received the B. Eng. degree in Electrical Engineering from China University of Mining and Technology, Jiangsu, China, in 2005, the M. Sc. Degree in Electrical Engineering from Shanghai Jiao Tong University, Shanghai, China, in 2008, and the Ph. D. degree in Energy Technology from the Department of Energy Technology, Aalborg University, Aalborg, Denmark, in 2012.

He joined the Southeast University in 2017 as a Professor in the School of Electrical Engineering, Southeast University, Nanjing, China. From 2013 to 2015 and from 2015 to 2017, he was a Postdoctoral Researcher and an Assistant Professor, respectively, in the Department of Energy Technology, Aalborg University, Aalborg, Denmark. His main research interests include wind power generation, multilevel converters, high-voltage direct-current technology, DC grid and offshore wind farm-power systems dynamics.

**Qiang Yu** received the B.S. degree in electrical engineering from Jilin University, Changchun, China, in 2017. He is currently working toward the Ph.D. degree in School of Electrical Engineering, Southeast University, Nanjing, China.

His research interests include modular multilevel converter and high-voltage direct current technology.

**Yanbo Wang** (S'05-M'07-SM'19) received Ph.D. degree in the Department of Energy Technology, Aalborg University, Denmark, in 2017. Currently, he is with the Department of Energy Technology in Aalborg University as an Assistant Professor. From June to October of 2016, he was a visiting scholar in Power System Research Group of the Department of Electrical and Computer Engineering, University of Manitoba, Winnipeg, MB, Canada. His research interests include distributed power generation system, wind power system, microgrid, as well as operation and control technologies of power electronic-dominated power system.

Dr.Wang's paper on Distributed Power System received the First Prize Paper Award of the 6th International Conference of Smart Grid cosponsored by IEEE Industry Application Society in 2018. He received the Best Session Paper Award at the annual conference of the IEEE Industrial Electronics Society in 2015 in Japan.

**Frede Blaabjerg** (S'86–M'88–SM'97–F'03) was with ABB-Scandia, Randers, Denmark, from 1987 to 1988. From 1988 to 1992, he got the PhD degree in Electrical Engineering at Aalborg University in 1995. He became an Assistant Professor in 1992, an Associate Professor in 1996, and a Full Professor of power electronics and drives in 1998. From 2017 he became a Villum Investigator. He is honoris causa at University Politehnica Timisoara (UPT), Romania and Tallinn Technical University (TTU) in Estonia.

His current research interests include power electronics and its applications such as in wind turbines, PV systems, reliability, harmonics and adjustable speed drives. He has published more than 600 journal papers in the fields of power electronics and its applications. He is the co-author of four monographs and editor of ten books in power electronics and its applications.

He has received 32 IEEE Prize Paper Awards, the IEEE PELS Distinguished Service Award in 2009, the EPE-PEMC Council Award in 2010, the IEEE William E. Newell Power Electronics Award 2014, the Villum Kann Rasmussen Research Award 2014, the Global Energy Prize in 2019 and the 2020 IEEE Edison Medal. He was the Editor-in-Chief of the IEEE TRANSACTIONS ON POWER ELECTRONICS from 2006 to 2012. He has been Distinguished Lecturer for the IEEE Power Electronics Society from 2005 to 2007 and for the IEEE Industry Applications Society from 2010 to 2011 as well as 2017 to 2018. In 2019-2020 he serves a President of IEEE Power Electronics Society. He is Vice-President of the Danish Academy of Technical Sciences too.

He is nominated in 2014-2019 by Thomson Reuters to be between the most 250 cited researchers in Engineering in the world.

**Xu Cai** received the B. Eng. degree from Southeast University, Nanjing, China, in 1983, and the M. Eng. and Ph.D. degrees from China University of Mining and Technology, Jiangsu, China, in 1988 and 2000, respectively, all in electrical engineering.

He was with the Department of Electrical Engineering, China University of Mining and Technology, as an Associate Professor from 1989 to 2001. Since 2002, he has been a Professor with Shanghai Jiao Tong University, Shanghai, where he has also been the Director of the Wind Power Research Center since 2008. He was the Vice Director of the State Energy Smart Grid R&D Center, Shanghai, China, from 2010 to 2013. His current research interests include power electronics and renewable energy exploitation and utilization, including wind power converters, wind turbine control system, large power battery storage systems, clustering of wind farms and its control system, and grid integration.